






RESEARCH ARTICLE | SEPTEMBER 05 2023

# Pore-scale study of miscible density instability with viscosity contrast in porous media

Jin Chen (陈进) ; Geng Wang (王耿); Junyu Yang (杨君宇); Timan Lei (雷体蔓)    
Kai H. Luo (罗开红)  



*Physics of Fluids* 35, 094104 (2023)  
<https://doi.org/10.1063/5.0161872>



View  
Online



Export  
Citation

CrossMark

## Articles You May Be Interested In

Shapes of a rising miscible droplet

*Physics of Fluids* (January 2020)

Competition of gravity and viscous forces in miscible vertical displacement in a three-dimensional porous medium

*Physics of Fluids* (July 2022)

Experimental and numerical investigation of a density-driven instability during a horizontal miscible displacement

*Physics of Fluids* (June 2023)

# Pore-scale study of miscible density instability with viscosity contrast in porous media

Cite as: Phys. Fluids **35**, 094104 (2023); doi: [10.1063/5.0161872](https://doi.org/10.1063/5.0161872)

Submitted: 12 June 2023 · Accepted: 16 August 2023 ·

Published Online: 5 September 2023



View Online



Export Citation



CrossMark

Jin Chen (陈进), Geng Wang (王耿), Junyu Yang (杨君宇), Timan Lei (雷体蔓), <sup>a)</sup> and Kai H. Luo (罗开红) <sup>a)</sup>

## AFFILIATIONS

Department of Mechanical Engineering, University College London, Torrington Place, London WC1E 7JE, United Kingdom

<sup>a)</sup> Authors to whom correspondence should be addressed: [t.lei@ucl.ac.uk](mailto:t.lei@ucl.ac.uk) and [k.luo@ucl.ac.uk](mailto:k.luo@ucl.ac.uk)

## ABSTRACT

The transport of miscible fluids in porous media is a prevalent phenomenon that occurs in various natural and industrial contexts. However, this fundamental phenomenon is usually coupled with interface instabilities (e.g., viscous/density fingering), which has yet to be thoroughly investigated. In this paper, a multiple-relaxation-time lattice Boltzmann method is applied to study the displacement between two miscible fluids in porous media at the pore scale, with the coexistence of density difference (Rayleigh number  $Ra$ ), viscosity contrast ( $R$ ), and injection velocity ( $U_{top}$ ). A parametric study is conducted to evaluate the impact of  $Ra$ ,  $R$ , and  $U_{top}$  on the flow stability. For a fixed  $Ra$  that can trigger density fingering, the increase in  $R$  or  $U_{top}$  is found to suppress density fingering. Consequently, under a large  $U_{top}$  and a moderate  $R$ , the density fingering is fully stabilized and the flow follows a stable pattern. Furthermore, as both  $R$  and  $U_{top}$  grow to a sufficiently high level, they can jointly trigger viscous fingering. In addition, the increasing  $Ra$  shows an enhancing effect on both density fingering and viscous fingering. Finally, by quantitatively analyzing the fingering length ( $l_m$ ) and the fingering propagation time ( $t_e$ ), five different flow patterns are classified as viscosity-suppressed (I), viscosity-enhanced (II), viscosity-unstable (III), displacement-suppressed (IV), and stable (V) regimes. In a three-dimensional parameter space spanned by  $Ra$ ,  $R$ , and  $U_{top}$ , the parameter ranges of the five regimes are determined according to  $l_m$  and  $t_e$ . These findings hold a significant value in providing guidance for controlling the flow stability by selecting appropriate operating conditions.

© 2023 Author(s). All article content, except where otherwise noted, is licensed under a Creative Commons Attribution (CC BY) license (<http://creativecommons.org/licenses/by/4.0/>). <https://doi.org/10.1063/5.0161872>

## I. INTRODUCTION

Carbon dioxide ( $CO_2$ ) emission has been an increasing concern due to its role as a main source of greenhouse gases, which cause global warming, iceberg melting, and sea level increasing.<sup>1,2</sup> Among the known technologies for reducing  $CO_2$  emissions, carbon capture and storage (CCS) is one of the most promising methods in terms of cost and scale.<sup>3</sup> Deep saline aquifers are the most popular storage sites due to their large space and availability.<sup>4</sup> In CCS,  $CO_2$  is injected into the aquifer and gradually dissolved into the brine.<sup>5</sup> The  $CO_2$  dissolution slightly increases the brine density, thus introducing a buoyantly unstable stratification of a denser  $CO_2$ -enriched brine on top of the fresh brine.<sup>6,7</sup> Such a stratification finally triggers density instability accompanied by strong convection, which plays a significant role in enhancing the dissolution and spreading of  $CO_2$  into the aquifers.<sup>8,9</sup> Meanwhile, aside from the increasing effect on density, the dissolution of  $CO_2$  also modifies the fluid viscosity.<sup>10</sup> The viscosity contrast can greatly affect the onset and development of density fingering.<sup>11</sup> Therefore, it is essential to study density instability with viscosity contrast in porous media to enhance the understanding of CCS.

Density-driven convection under the context of  $CO_2$  storage has been extensively studied experimentally, numerically, and theoretically.<sup>12–21</sup> Experiments were performed in Hele–Shaw cells, micromodels, sand packs, or cores to identify density instability patterns and analyze the underlying mechanisms.<sup>16,17,22</sup> The key factors for accelerating fluid transport and affecting fluid mixing were discussed.<sup>13</sup> However, these experiments were hard to exactly control the configuration of porous media or concentration perturbations, which might greatly influence the instability pattern.<sup>21</sup> Moreover, experiments were generally time-consuming, costly, and highly subjective to human and equipment capacities.<sup>13</sup> Theoretical analysis played an important role in predicting possible instabilities. Many theoretical studies have been reported based on the linear stability analysis and the scaling analysis.<sup>18,19,23–31</sup> These theoretical analyses focused on predicting the onset of fingering via analyzing the growth rate of initial perturbations, which were able to cover the possible instability scenarios at an initial stage before nonlinear behaviors happen.<sup>18</sup> For viscous fingering with gravitational force, the concept of critical velocity was proposed to decide the velocity bounds for stability or instability.<sup>28–31</sup> However,

theoretical studies could not describe the whole-life behaviors of density instability.

Numerical simulations are helpful to understanding the CO<sub>2</sub> dissolution and transport behaviors during CCS. For such a process, numerical studies were conducted to investigate mechanisms of both density and viscous instabilities. For density fingering, the whole-life behaviors of fingering development in porous media were simulated and it was revealed that the nonlinear interactions of fingers exert a substantial influence on both the speed of front propagation and the overall mixing.<sup>18</sup> Four development stages were identified as diffusion, early convection, late convection, and convection shutdown.<sup>32</sup> The flux growth regime was further divided into two sub-regimes: the early flux growth regime caused by tiny fingers and the late flux growth regime caused by the nonlinear perturbations.<sup>21</sup> The nonlinear interactions between chemical reactions and density fingering were studied.<sup>33</sup> Moreover, the effects of perturbations and porous media ignored in experiments were also reported in numerical simulations.<sup>15,24</sup> In CCS, the density instability caused by the dissolution of CO<sub>2</sub> results in an acceleration of mass transport between fluids, thus reducing the time required for CO<sub>2</sub> storage.<sup>34</sup> As for viscous fingering, the viscosity contrast was found to introduce mobility differences and thus yield viscous fingering phenomena between two displacement fluids.<sup>35</sup> The nonlinear phenomena of shielding and spreading were observed in simulations, together with the tip splitting in miscible displacement first reported by Tan and Homsy.<sup>36</sup> Furthermore, the calculated metric of mixing length, serving as an indicator of fingering development, was found to grow linearly over time.<sup>37</sup> The viscosity ratio was then reported to play a significant role in influencing the fingering onset and the fingering dynamics.<sup>20,35,38–42</sup> Larger viscosity ratios were found to delay the fingering onset but result in an increased number of fingers with smaller characteristic wavelength.<sup>43</sup> Similar to density fingering, the development of viscous fingering was divided into different stages according to the fingering's full-lifecycle.<sup>42</sup> Moreover, within the context of CCS, viscous fingering was observed to introduce flow channels for CO<sub>2</sub> leakage, yet simultaneously induce strong convection for enhancing fluid dissolution.<sup>42</sup> Effects of media heterogeneity, magnetic field, and nanoparticles on the development of viscous fingering were explored.<sup>39–41</sup> Chemical reactions were found to have complex effects on viscous fingering by changing both the fluid concentration and the media porosity.<sup>20,38,44,45</sup>

The above studies provide much insight into density and viscous instabilities in porous media. However, there remain two main problems. On the one hand, all the above research is considered either density fingering or viscous fingering, which included density or viscosity contrasts. In applications of CCS, however, the dissolution of CO<sub>2</sub> modifies both fluid density and viscosity, thus introducing differences in both density and viscosity between the displacing and displaced fluids. There exist some studies on density-driven convection coupled with viscosity contrast through experimental observations.<sup>11,46</sup> It was reported that viscosity contrast played an important role in convective mixing by changing the dissolution rate and onset time.<sup>46</sup> Different fingering structures and dissolution behaviors were observed for different viscosity ratios. However, the inherent limitations of experiments restricted the available parameters in experiments, and thus the mechanism underlying the density fingering with viscosity contrast was not fully investigated. On the other hand, due to the complicated structure of porous media, current numerical studies were mainly based on

volume-averaged scales, like representative elementary volume scale or Darcy scale. A pioneering study was conducted, utilizing a Hartley-transform-based pseudospectral method to simulate the situations when viscosity and density contrasts have opposite effects on stability.<sup>27</sup> However, these volume-average studies were likely to introduce errors if without pore-scale information.<sup>47</sup> Therefore, a pore-scale study is needed to show the details of density fingering with viscosity contrast.

This study is aimed at providing a pore-scale simulation of density instability with the coexistence of viscosity contrast, thereby getting a deeper understanding of how the viscosity contrast affects instability development and then the fluid dissolution. In addition, the effects of injection velocity of the top layer are also investigated in this paper as an innovative attempt. During the past decades, the lattice Boltzmann method (LBM) has become a powerful solver for simulating fluid flows in porous media at the pore scale. This is attributed to its advantages in parallel computing and handling complex boundaries.<sup>48</sup> In this study, a multiple-relaxation-time (MRT) lattice Boltzmann (LB) method is utilized to solve the governing equations and the nonequilibrium extrapolation method, and the halfway bounce-back method are used to deal with the boundary conditions.

## II. CONFIGURATION

As shown in Fig. 1, the computational domain is a homogeneous 2D system with length  $l_x$  and width  $l_y$ . A set of uniformly distributed solid grains is utilized inside the domain to simulate the porous structure in reality. The detailed location and size settings for these grains are shown in Fig. 1. In order to study the fingering phenomenon under the effects of gravity, viscosity difference, and injection velocity, two fluids (labeled as fluid 1 and fluid 2) are introduced in this system. These two fluids are considered miscible, nonreactive, isothermal, and incompressible. Initially, fluid 2 without solute A suffuses the whole domain. Then, fluid 1 with solute A at a concentration of  $C_0$  is injected into the system from the top. The injection velocity is  $U_0$ . Notably, a concentration disturbance is applied to help trigger the fingering phenomenon. In this research, the dissolution of species A is assumed to modify both the fluid density and viscosity.

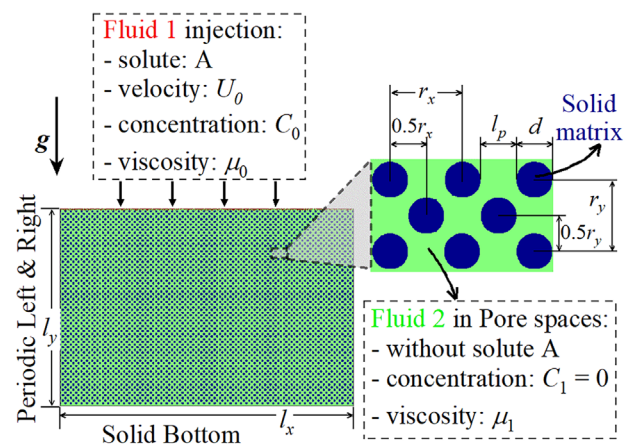


FIG. 1. The model schematic: two miscible fluids with viscosity contrast and injection velocity in porous media.

### III. GOVERNING EQUATIONS

The governing equations for the fluid flow and species transport are described by the Navier–Stokes equations and the convection–diffusion equation as follows:

$$\begin{aligned} \nabla \cdot \mathbf{u} &= 0, \\ \rho_0 \left( \frac{\partial \mathbf{u}}{\partial t} + \mathbf{u} \cdot \nabla \mathbf{u} \right) &= -\nabla p + \nabla \cdot (\mu \nabla \mathbf{u}) + \mathbf{F}, \\ \frac{\partial C}{\partial t} + \mathbf{u} \cdot \nabla C &= D \nabla^2 C, \end{aligned} \quad (1)$$

where  $\mathbf{u} = (u, v)$  is the velocity,  $\rho_0$  is the density,  $t$  is the time,  $p$  is the pressure,  $\mu = \rho_0 \nu$  is the fluid dynamic viscosity with  $\nu$  being the fluid kinematic viscosity,  $C$  is the concentration, and  $D$  is the diffusion coefficient.  $\mathbf{F}$  is the force applied to the flow, which is introduced by gravity difference. According to the Boussinesq approximation, fluid density is assumed as a constant  $\rho_0$  except in the force term  $\mathbf{F}$ . The gravity acceleration term caused by the concentration  $C$  is defined as<sup>49</sup>

$$\mathbf{F} = (0, F_y) = (0, g\rho_0(1 + \beta C)), \quad (2)$$

where  $g$  is the gravity and  $\beta$  is the concentration expansion coefficient. Moreover, the fluid viscosity  $\mu$  is also decided by the concentration evolution. The viscosity is assumed to follow an exponential law with the local concentration  $C$  as<sup>50</sup>

$$\mu = \mu_1 \exp\left(-\frac{C}{C_0} R\right), \quad (3)$$

where  $R = \ln(\mu_1/\mu_0)$  is the viscosity ratio, and  $\mu_0$  and  $\mu_1$  are the dynamic viscosities of fluid 1 ( $C = C_0 = 1$ ) and fluid 2 ( $C = C_1 = 0$ ), respectively. As for the boundary conditions, no-slip and no-flux conditions are applied to the grains inside the system. The lateral boundaries of the system are set as periodic. The top boundary is defined by the prescribed velocity and concentration. The bottom boundary is defined by the no-slip condition and given concentration. In summary, these boundary conditions are described as

$$\begin{aligned} \mathbf{u}(x_g, y_g) &= (0, 0), \quad \nabla C(x_g, y_g) = (0, 0), \\ \mathbf{u}(0, y) &= \mathbf{u}(l_x, y), \quad C(0, y) = C(l_x, y), \\ \mathbf{u}(x, l_y) &= (0, -U_0), \quad C(x, l_y) = C_0, \\ \mathbf{u}(x, 0) &= (0, 0), \quad \nabla C(x, 0) = (0, 0), \end{aligned} \quad (4)$$

where  $(x_g, y_g)$  is the surface of solid grains and  $U_0$  is the injection velocity of fluid 1.

In order to introduce dimensionless parameters, the characteristic length, velocity, and concentration are selected, respectively, as

$$L = l_x, \quad U = \sqrt{g\beta L \Delta C}, \quad C_{ch} = C_0. \quad (5)$$

The nondimensional parameters are as

$$\begin{aligned} t^* &= \frac{t}{L/U}, \quad C^* = \frac{C}{C_0}, \quad \rho^* = \frac{\rho - \rho_0}{\rho_0 \beta}, \\ \text{Ra} &= \frac{L^3 g \beta (C_0 - C_1)}{\nu D}, \quad \text{Sc} = \frac{\nu}{D}, \quad U_{\text{top}} = \frac{U_0}{U}. \end{aligned} \quad (6)$$

The key parameters in this project are the Rayleigh number  $\text{Ra}$ , the viscosity ratio  $R$ , the top flow velocity  $U_{\text{top}}$ , and the Schmidt number  $\text{Sc}$ . The nondimensional injection velocity of the top flow  $U_{\text{top}}$  is called the injection velocity for convenience in Secs. IV A–IV C.

In this work, the multiple-relaxation-time (MRT) LB method is utilized to solve the above governing equations and boundary conditions.<sup>51</sup> The details of the models are shown in the Appendix.

### IV. RESULTS AND DISCUSSION

In this part, the density instability with viscosity contrast is simulated for different injection velocities in a homogeneous porous medium. For the computational domain in Fig. 1, the geometric parameters are set as  $l_x = 1$ ,  $l_y = 0.672$ ,  $d = 0.00806$ ,  $r_x = r_y = 0.0181$ , and the medium porosity is calculated as  $\phi = 1 - \pi d^2 / 2r_x r_y = 0.670$ . It is worth mentioning that the present pore-scale study is able to capture representative features, and all typical phenomena of fingering are observed, including merging, shielding, tip splitting, and finger reinitiation. Therefore, the simulation results at pore scales are of relevance at larger scales. In this study, the Schmidt number is fixed as  $\text{Sc} = 100$ , and different values of Rayleigh number  $\text{Ra}$ , viscosity ratio  $R$ , and injection velocity  $U_{\text{top}}$  are selected to change the simulation conditions. After grid convergence tests, a mesh of size  $N_x \times N_y = 1488 \times 1000$  is utilized in this research. It is noted that all the simulations use the same initial concentration distribution to exclude the effects of perturbations.<sup>24</sup> Throughout this paper, all the parameters are set in lattice units. Each test continues until the fingering front (i.e., the front position of fluid 1,  $l_f$ ) reaches the position  $l_f = 0.75l_y$ . More details about model validation can be found in the supplementary material.

#### A. General pattern analysis

To get a comprehensive understanding of the density fingering phenomena with viscosity contrast at the pore scale, simulations of fingering patterns are conducted for different parameters. For illustration, two sets of simulation cases are discussed: cases I(a)–I(c) without injection velocity and cases II(a)–II(c) with injection velocity. The detailed simulation parameters are listed in Table I.

##### 1. Without injection velocity ( $U_{\text{top}}=0$ )

In cases I(a)–I(c), the injection velocity is excluded from consideration. The Rayleigh number is set as  $\text{Ra} = 10^9$ , which is large enough to trigger the density fingering phenomenon. The viscosity ratio  $R$  is set as 0, 3, and  $-3$  for cases I(a), I(b), and I(c), respectively. For each case, Fig. 2 shows the contours of density fields  $\rho^*$  at different time instants  $t^*$ , with each row of contours reaching the same front position  $l_f$ .

It is found that all three cases display a classical fingering development pattern, regardless of the viscosity contrast value.<sup>21,32,42</sup> Initially, the spreading of solute A is dominated by diffusion as a planar. With the accumulation of A in the top layer, the density difference between the A-accumulated top layer and the host fresh layer eventually gets large enough to trigger the onset of tiny fingers. These fingers

TABLE I. Parameters for case I and II in Part A.

Tests	Rayleigh number $\text{Ra}$	Injection velocity $U_{\text{top}}$	Viscosity ratio $R$
Cases I(a)–I(c)	$10^9$	0	[−3,3]
Cases II(a)–II(c)		$10^{-2}$	[−3,3]



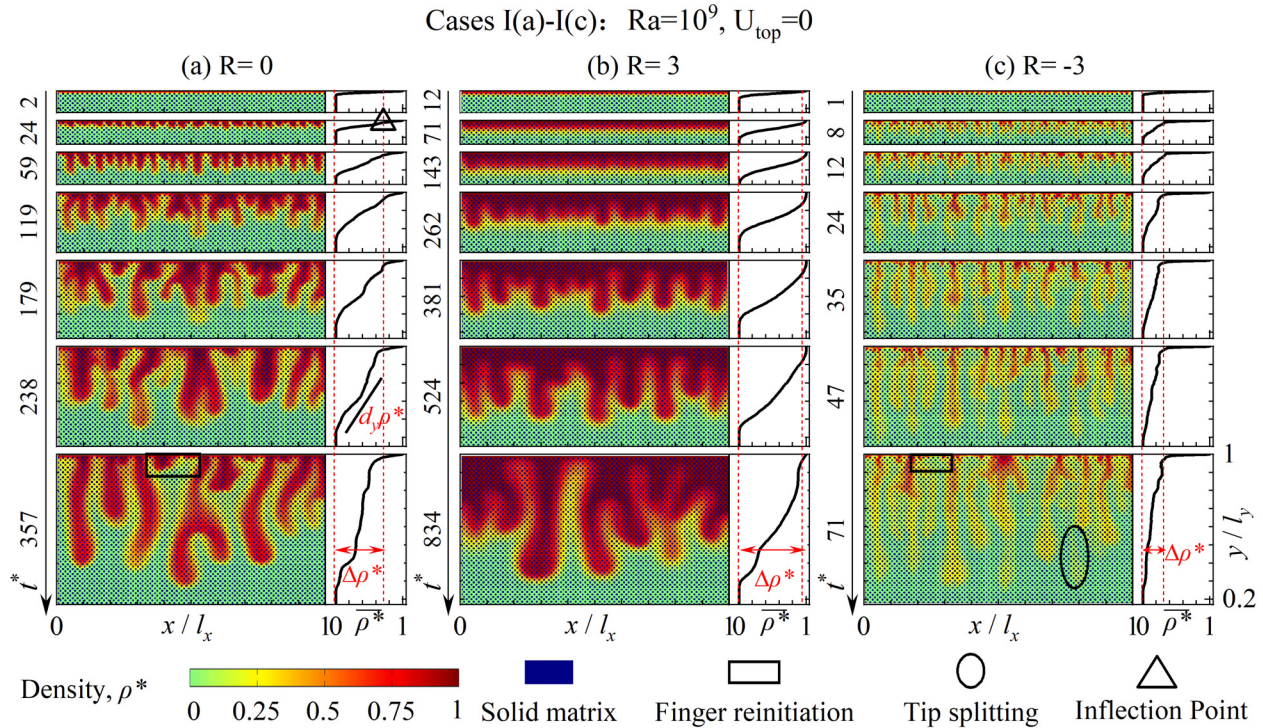


FIG. 2. Contours of density  $\rho^*$  and transversely averaged density  $\bar{\rho}^*$  for cases I: (a)  $R = 0$ , (b)  $R = 3$ , and (c)  $R = -3$ .

keep growing and start to interact nonlinearly with each other. Finally, after experiencing a merging state, several strong fingers are left to dominate the flow. Typical phenomena of fingering in miscible displacement are observed in Fig. 2, like dominant fingers' spreading and shielding and tip splitting.<sup>36</sup>

Although these three cases share a similar fingering development pattern, three differences among them are observed due to varied viscosity ratios. First, finger re-initiation and tip splitting are enhanced in case I(c), while they are suppressed in case I(b), which are marked by rectangles and ellipses in Fig. 2, respectively. This stems from the fact that, as  $R$  increases, the displaced fluid (i.e., fluid 2) manifests larger viscosity and thus suppresses finger re-initiation and tip splitting. Second, the time period each case takes to reach the same front position  $l_f$  varies. Comparing the non-dimensional time  $t^*$  for each front position, it is evident that the ascending  $R$  slows down the propagation of solute A along the direction of gravity. For example, from cases I(c) via I(a) to I(b), it takes  $t^* = 71, 357$  and  $834$ , respectively, for the fingering front to reach the position  $l_f = 0.75l_y$ . This is straightforward as a larger  $R$  represents a more viscous fluid 2, which in turn causes a larger resistance force as fluid 1 tries to spread into fluid 2. Finally, with the increase in  $R$ , the enhanced accumulation of A in the top layer is detected, which subsequently brings about the amplified density jump  $\Delta\rho^*$  and buoyance force  $F$ .

After qualitative discussions of similarities and differences between the three cases I(a)–I(c), quantitative analyses are further set out to provide a deep understanding of density instability with viscosity contrast. For such a purpose, the horizontally averaged density is calculated as

$$\bar{\rho}^* = \frac{1}{l_x} \int_0^{l_x} \rho^* dx. \quad (7)$$

In Fig. 2, the horizontally averaged density  $\bar{\rho}^*$  is plotted on the right side of each contour field. From profiles of  $\bar{\rho}^*$  in each case, the line slope [e.g., marked as  $d_y \rho^*$  at  $t^* = 238$  in case I(a)] is found to decrease with time. This is attributed to the fact that fingering spreads downward and accelerates the dissolution of species A. In the meantime, as  $\bar{\rho}^*$  starts to decrease along the  $y$  direction (or  $d_y \rho^*$  is no longer infinite), an inflection point is observed in each profile of  $\bar{\rho}^*$  [e.g., marked by a triangle at  $t^* = 24$  in case I(a)]. Accordingly, the density jump  $\Delta\rho^*$  between the A-accumulated top layer and the host fresh layer can be determined from profiles of  $\bar{\rho}^*$ . As denoted in Fig. 2,  $\Delta\rho^*$  is calculated as the density difference from the inflection point to the host fluid density level. It is apparent that  $\Delta\rho^*$  determines the buoyance force  $F$  and subsequently the onset and development of density fingering. From Fig. 2, it is confirmed that the rise in  $R$  causes a growth in  $\Delta\rho^*$  or  $F$ . This can be explained from the aspect of force balance. With the growing  $R$ , the enlarged viscosity force requires a large  $\Delta\rho^*$  or  $F$  to be balanced. The relationship between  $R$  and  $\Delta\rho^*$  (or  $F$ ) can also be understood from the perspective of Taylor dispersion. Taylor dispersion refers to the phenomenon of effective mixing and diffusion that occurs in a shear flow with a concentration gradient.<sup>32</sup> In case I, increasing  $R$  hinders the spreading velocity of solute A, which, in turn, weakens the intensity of Taylor dispersion. The weakened dispersion causes larger concentration inside the fingers. Therefore, increasing  $R$  generates a large  $\Delta\rho^*$ . However, it is notable that the simulation in this work ends at  $l_f/l_y$ ,

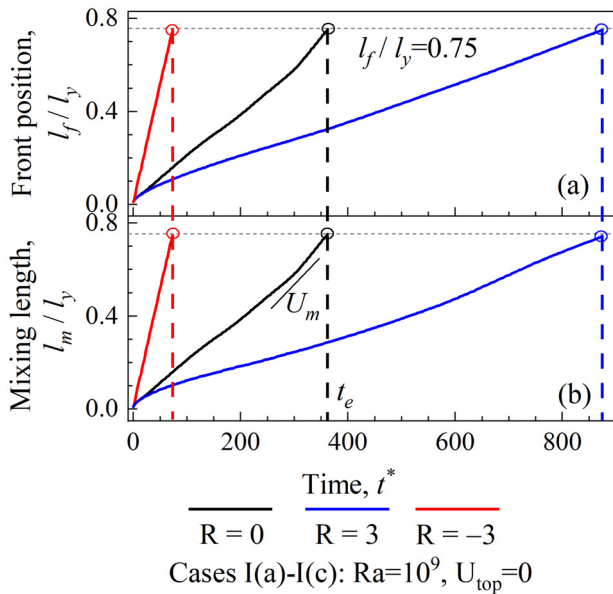


FIG. 3. Temporal evolutions of (a) the front position  $l_f/l_y$  and (b) mixing length  $l_m/l_y$  for cases I(a)–I(c) with  $Ra = 10^9, U_{top} = 0$ , and  $R = 0, 3, -3$ .

$= 0.75$  with flow dominated by advection, while from a previous study,<sup>52</sup> Taylor dispersion becomes independent of  $R$  at the very late stage when the flow is dominated by dispersion instead of advection.

On the other hand, two important metrics are introduced based on profiles of  $\rho^*$  to quantify the development of density fingering.

First, the fingering front  $l_f$  is defined as the position where  $\bar{\rho}^* = 0.01$ . Second, the mixing length (or fingering length)  $l_m$  is calculated as the distance between  $\bar{\rho}^* = 0.99$  and  $\bar{\rho}^* = 0.01$ . Temporal evolutions of the front position  $l_f/l_y$  and mixing length  $l_m/l_y$  for cases I(a)–I(c) are depicted in Fig. 3. Each simulation stops when  $l_f/l_y = 0.75$ , and the corresponding time is termed as the end time,  $t_e$ . In cases I(a)–I(c) with  $U_{top} = 0$ ,  $t_e$  is observed to increase with the growing  $R$ , which identifies the slow spreading of species A. This is expected since the large  $R$  introduces the strong viscous resistance to suppress the fingering development driven by the buoyance force  $F$ . As for temporal evolutions of the mixing length  $l_m/l_y$ , profiles are similar to those of  $l_f/l_y$ . The reason is that, in cases I(a)–I(c) with  $U_{top} = 0$ , no additional force except for the buoyance force is applied to drive the movement of fluid 1. Therefore, density fingering starts almost from the top boundary and  $l_m$  is the same as  $l_f$ . Moreover, it is observed that, after the initial diffusion stage,  $l_m$  changes to grow at an almost constant rate due to the appearance of density fingering, which is consistent with previous studies.<sup>36,37</sup> Accordingly, as denoted in Fig. 3, the slope of  $l_m$  during the fingering development stage is defined as the fingering growth velocity  $U_m$ . From profiles of  $l_m$ ,  $U_m$  is found to have a negative correlation relationship with  $R$  in cases I(a)–I(c). This is attributed to the suppressing effect of large  $R$  on the fingering development.

2. With injection velocity ( $U_{top}=10^{-2}$ )

In cases II(a) and II(b), an additional injection velocity is introduced as  $U_{top} = 10^{-2}$ , while the Rayleigh number and the viscosity ratio are identical to those of cases I(a)–I(c), namely,  $Ra = 10^9$  and  $R = 0, 3, -3$ . Similarly, the contours of density fields  $\rho^*$  for cases II are displayed in Fig. 4.

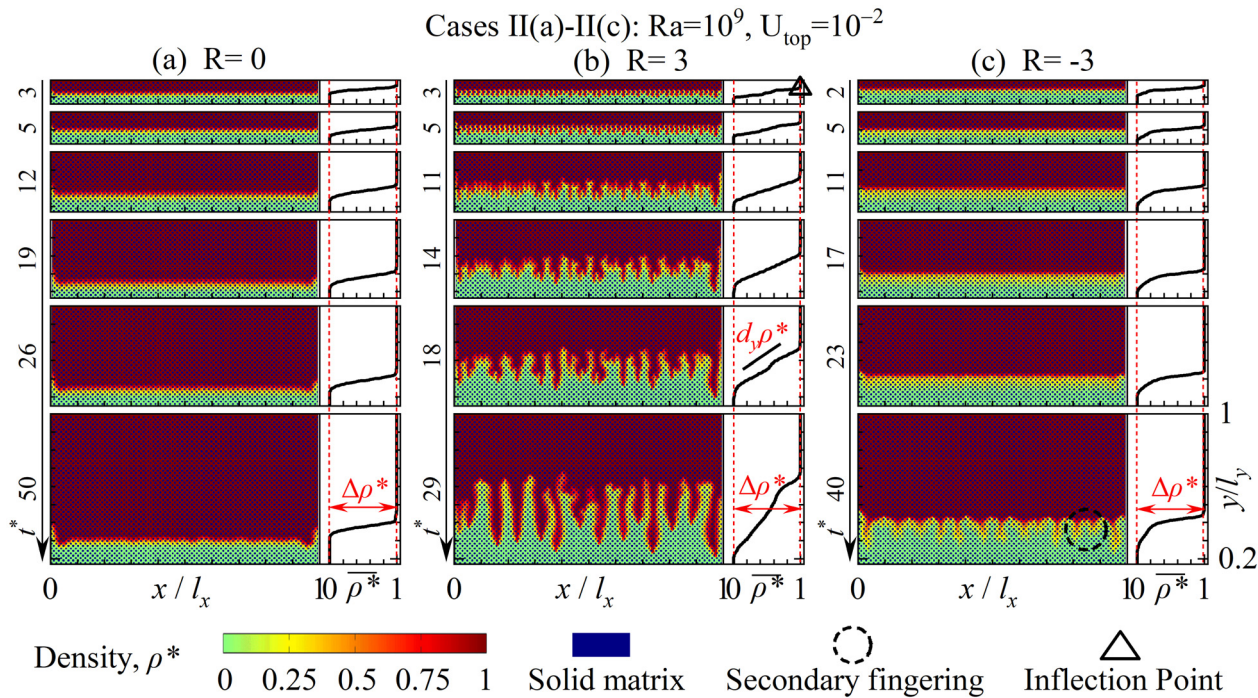


FIG. 4. Contours of density  $\rho^*$  and transversely averaged density  $\bar{\rho}^*$  for cases II (a)  $R = 0$ , (b)  $R = 3$ , and (c)  $R = -3$ .



The fingering development patterns in cases II exhibit a distinct divergence from those observed in cases I. In case II(a) where  $R = 0$ , the system maintains stable throughout the simulation life span. Conversely, in cases II(b) and II(c) with non-zero  $R$ , the onset and development of density fingering are observed. In case II(b) with a high viscosity ratio  $R = 3$ , fingers appear at an early stage. The difference between cases II(a) and II(b) reveals that fingers in case II(b) are introduced by the combination of injection velocity and viscosity ratio, which are thus referred to as viscous fingering. On the other hand, in case II(c) with a small viscosity ratio  $R = -3$ , the system remains stable for a long period. Upon the fingering front reaching  $0.75l_y$ , the flow in case II(c) undergoes instability and produces minuscule fingers, as denoted by dotted circles in Fig. 4. Therefore, upon examining the contours of  $R = -3, 0, \text{ and } 3$ , the flow field transitions from an unstable regime to a stable one and ultimately reverts to an unstable state. By comparing with cases I, the flow states in cases II indicate that the injection velocity serves to suppress the development of density fingering but enhance that of viscous fingering as  $R > 0$ .

In addition to fingering patterns, the injection velocity is observed to accelerate the spreading of solute A. Upon examining the time instant  $t^*$  when  $l_f$  reaches the same position, it is apparent that  $t^*$  is significantly smaller in cases II as compared to that in cases I. For example, it takes  $t^* = 71$  in case I(a) but  $t^* = 50$  in case II(a) for the fingering front to reach  $l_f = 0.75l_y$ . In addition, a comparison of the fluid transport speed among cases II(a)–II(c) demonstrates that the increasing  $R$  decelerates the fluid propagation velocity as  $R < 0$ , which is consistent with cases I. In contrast to cases I, as  $R$  increases to be  $R > 0$ , the higher  $R$  changes to accelerate fluid transport and the case II(b) with  $R = 3$  shows the fastest transport velocity among cases II. This discrepancy is attributed to the fact that the injection velocity and large viscosity  $R = 3$  in case II(b) bring about viscous fingering. Fingering is known to expedite fluid transport, and therefore, even though a higher viscosity ratio generates the stronger viscous resistance in case II(b), the intensified spreading by fingering surpasses the delaying effect induced by the viscous resistance.

Following qualitative discussions of fingering properties in cases II, quantitative analyses are conducted to comprehend the understanding of density instability with injection velocity. Again, the horizontally averaged density  $\bar{\rho}^*$  is graphed on the right side of each contour plot. For each profile of  $\bar{\rho}^*$  in Fig. 4, an inflection point is identified and then the density jumps  $\Delta\rho^*$  (or the buoyance force  $F$ ) can be obtained. Different from cases I, values of  $\Delta\rho^*$  in cases II(a)–II(c) are almost the same and reach the maximum density jump  $\Delta\rho_m^* = 1$ . Although under  $\Delta\rho_m^*$ , density fingering is weak or even disappeared in cases II(c) and II(a). This verifies that the injection velocity  $U_{top}$  impedes the effects of  $F$  and subsequently suppresses the density fingering development.

Temporal evolutions of the aforementioned metrics  $l_f$  and  $l_m$  are plotted in Fig. 5 to quantify the fingering development with injection velocity in cases II. For each test, the simulation ends at  $t_e$  with  $l_f = 0.75l_y$ . Profiles of  $l_f$  are observed to increase with time following a similar trend as those in cases I. Each  $l_f$  increases progressively until the end time  $t_e$ . In cases II with  $U_{top} = 10^{-2}$ , as  $R$  increases,  $t_e$  is found to increase when  $R < 0$  but switches to decreases when  $R > 0$ . Different from cases I with the positive correlative between  $R$  and  $t_e$ , this nonmonotonical relationship between  $R$  and  $t_e$  in cases II evidences the enhancing effects of viscous fingering on fluid propagation

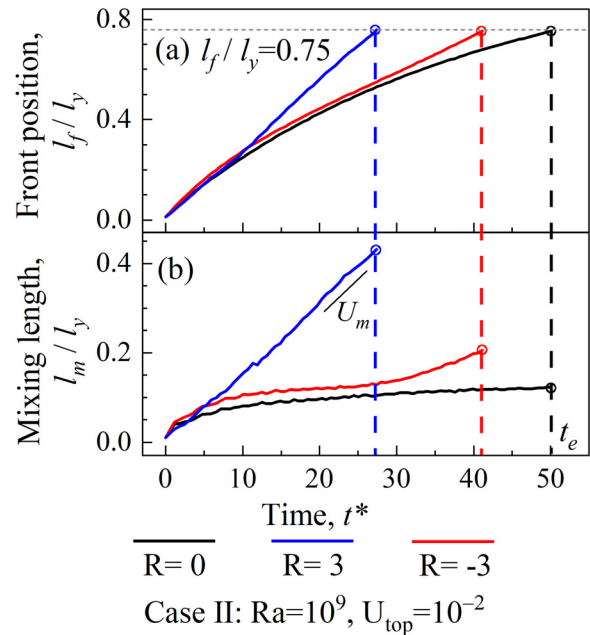
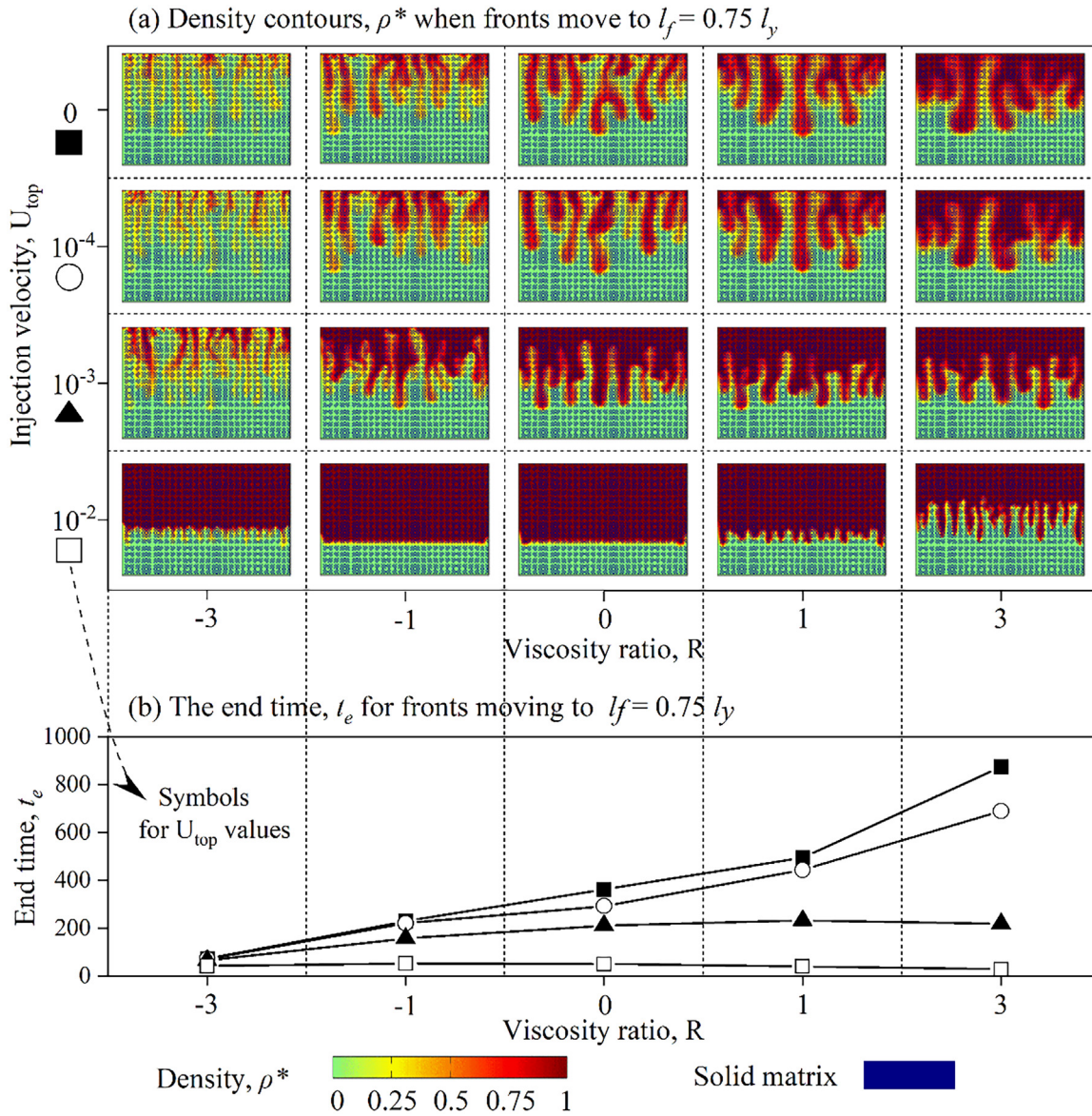


FIG. 5. Temporal evolutions of (a) front position  $l_f/l_y$  and (b) mixing length  $l_m/l_y$  for cases II(a)–II(c) with  $Ra = 10^9$ ,  $U_{top} = 10^{-2}$ , and  $R = 0, 3, -3$ .

velocity in case II (b) with  $R = 3$ . Another distinction from cases I is that, driven by the additional  $U_{top}$ , results for  $l_m$  exhibit a significant difference from those for  $l_f$ . In case II(a) ( $R = 0$ ),  $l_m$  follows a growth pattern dominated by diffusion with no fingering observed. Differently,  $l_m$  for case II(b) ( $R = 3$ ) departs from the diffusive tendency at an early stage and turns to increase rapidly due to the onset of viscous fingering, whereas  $l_m$  for case II(c) ( $R = -3$ ) does not deviate from the diffusive trend until a very late stage, indicating the weak density fingering, which is also in good agreement with previous study.<sup>27</sup> Therefore, the largest growth velocity of fingering,  $U_m$ , among cases II(a)–II(c) is found in case II(b) with  $R = 3$ . This is attributed to the fact that the injection velocity impedes the onset of density fingering but helps to trigger viscous fingering when  $R > 0$ .

### B. Effects of $R$ and $U_{top}$

Following a preliminary analysis of density fingering properties with viscosity contrast and injection velocity, effects of the two key parameters (i.e.,  $R$  and  $U_{top}$ ) are further investigated. To this end, a series of simulations are performed with a fixed  $Ra = 10^9$  and varying  $R$  and  $U_{top}$ . The simulated density contours at the time instant  $t_e$  when the fluid front reaches  $l_f = 0.75l_y$  are plotted in Fig. 6(a). These contours reveal a diverse array of fingering dynamics, including enhanced fingering, weak fingering, and stable interface. In tests with a small  $U_{top}$  (e.g.,  $10^{-4}$ ), the fluid remains unstable for various values of  $R$  and the increasing  $R$  suppresses the fingering intensity. However, as  $U_{top}$  increases to be efficiently large (e.g.,  $10^{-2}$ ), the fluid displacement becomes the dominant mechanism, which suppresses the development of density fingering. Under this condition, the growing  $R$  within the range  $R < 0$  aids in restraining the formation of density fingering and even yields a stable fluid interface. For instance, in tests with  $U_{top}$



**FIG. 6.** (a) Density contours  $\rho^*$  when fluid fronts move to  $l_f = 0.75l_y$ , for cases with  $Ra = 10^0$  and different values of  $U_{top}$  and  $R$ . (b) Plots of the end time  $t_e$  as a function of  $R$  for different  $U_{top}$ .

$= 10^{-2}$  and  $R = 0, -1$ , the system maintains a stable planar fluid interface. This phenomenon can be explained by the opposite effects of viscosity and density contrasts on stability by choosing a favorable injection velocity.<sup>27</sup> In the large- $U_{top}$  scenario, the density contrast serves to enhance instability, while the large  $U_{top}$  amplifies viscous forces and suppresses density instability. Upon  $U_{top}$  reaching a sufficiently large magnitude, the flow can be fully stabilized, and the bound velocity is defined as the critical velocity,  $U_c$ . For example, in test with  $R = -1$ ,  $U_c$  is located between  $10^{-3}$  and  $10^{-2}$ , since the flow is fully stabilized when  $U_{top}$  increases from  $10^{-3}$  to  $10^{-2}$ . It is notable that  $U_c$  varies with  $Ra$  (density contrast),  $R$  (viscosity contrast), and time.

However, as  $R$  increases to be positive (i.e.,  $R > 0$ ), the combination of large  $U_{top}$  and  $R$  is observed to introduce viscous fingering, as displayed in test with  $U_{top} = 10^{-2}$  and  $R = 3$ . On the other hand, at a fixed  $R$ , the increasing  $U_{top}$  is found to hinder density fingering while triggering viscous fingering if  $R$  is efficiently large (i.e.,  $R = 3$ ).

Additionally, Fig. 6(b) displays the time  $t_e$  required for the fluid front to reach the position  $l_f = 0.75l_y$ . A smaller value of  $t_e$  signifies a faster spreading speed. It is demonstrated that the rise in  $U_{top}$  leads to a reduction in  $t_e$ , thereby hastening the spreading speed of solute A. This can be explained by the fact that  $U_{top}$  accelerates the movement of the displacing fluid 1. In contrast, there is a negative correlation



between  $R$  and the spreading speed of  $A$  when  $U_{top}$  is relatively small (i.e.,  $U_{top} \leq 10^{-4}$ ). This negative correlation becomes marginal and even disappears as  $U_{top}$  increases (i.e.,  $U_{top} \geq 10^{-3}$ ). For instance, with the increasing  $R$  at  $U_{top} = 10^{-3}$ ,  $t_e$  increases at first and reaches the largest value at  $R = 0$  and turns to decrease after this maximum point. This is attributed to the appearance of viscous fingering in tests with large  $U_{top}$  and  $R$ .

To quantify the effects of  $R$ , the mixing length  $l_m$  and the growth velocity of fingering  $U_m$  at  $t_e$  when the front positions reach  $l_f = 0.75l_y$  are plotted in Fig. 7 as a function of  $R$  for different  $U_{top}$ . In Fig. 7, the data for  $U_{top} = 10^{-4}$  is omitted to facilitate readability, given its close resemblance to that for  $U_{top} = 0$ . The results reveal that effects of  $R$  on fingering properties depend on the magnitude of  $U_{top}$ . For a small  $U_{top}$  ( $U_{top} \leq 10^{-3}$ ), a negative correlation between  $l_m$  and  $R$  is evident. However, as  $U_{top}$  increases to  $U_{top} = 10^{-2}$ ,  $l_m$  exhibits a weak negative association with  $R$  as  $R < 0$ , but a strong positive correlation with  $R$  as  $R > 0$ . This stems from the fact that, although the large  $U_{top}$  or  $R$  individually can suppress density fingering, the combination of these two factors can serve as the driving force for the initiation of viscous fingering. With regard to  $U_m$ , as  $U_{top}$  is small ( $U_{top} \leq 10^{-3}$ ), a negative correlation between  $U_m$  and  $R$  is detected from Fig. 7. This correlation arises from the fact that the large  $R$  tends to postpone the onset of fingering. However, results at  $U_{top} = 10^{-2}$  exhibit a nonlinear association between  $U_m$  and  $R$ . Specifically,  $U_m$  decreases with the growing  $R$  as  $R < 0$ , but  $U_m$  experiences an increase as  $R > 0$ . For example, the significant rise in  $U_m$  was detected at  $R = 3$ . This nonlinear correlation further corroborates our earlier analysis that the large  $R$  suppresses density fingering, but the large  $U_{top}$  and  $R$  can trigger the appearance of viscous fingering.

Moreover, to quantify the effects of  $U_{top}$ , the mixing length  $l_m$  and the growth velocity of fingering  $U_m$  upon a front position of  $l_f = 0.75l_y$  are plotted in Fig. 8 as a function of  $U_{top}$  for different  $R$ . The results indicate that an increase in  $U_{top}$  generally leads to a reduction in  $l_m$ , which is attributed to the suppressing effect of  $U_{top}$  on density

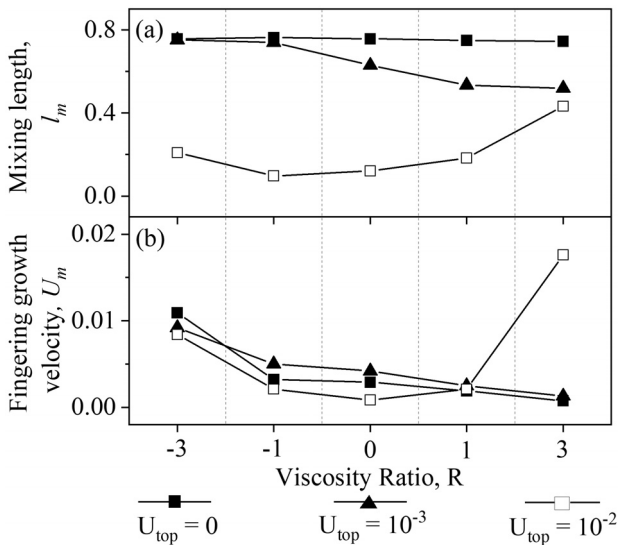


FIG. 7. Plots of (a) the mixing length  $l_m$  and (b) the growth velocity of fingering  $U_m$  when  $l_f = 0.75l_y$  as a function of  $R$  for different  $U_{top}$ .

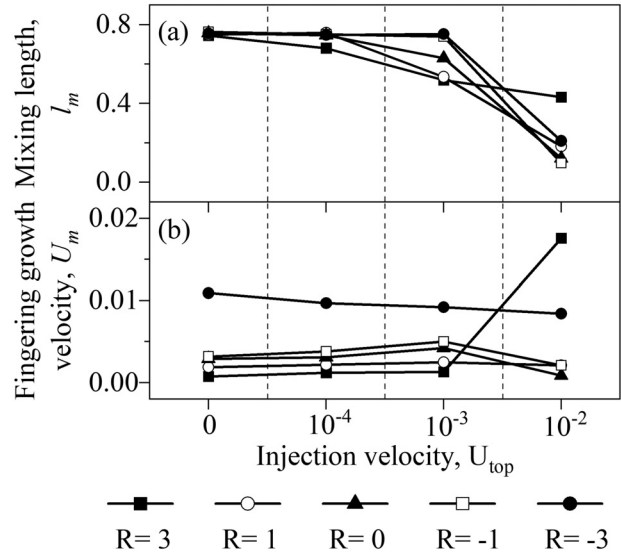


FIG. 8. Plots of (a) the mixing length  $l_m$  and (b) the growth velocity of fingering  $U_m$  when  $l_f = 0.75l_y$  as a function of  $U_{top}$  for different  $R$ .

fingering. The results reveal a negative correlation between  $U_{top}$  and  $l_m$ , which further corroborates the previous conclusion that  $U_{top}$  generally suppresses fingering. On the other hand, the results reveal that  $U_{top}$  has minimal impact on  $U_m$ , except in tests involving large  $U_{top}$  and  $R$ . For instance, a considerable surge in  $U_m$  is detected when  $U_{top}$  reaches  $U_{top} = 10^{-2}$  for  $R = 3$ . This phenomenon can be explained by the driving effect of large  $U_{top}$  and  $R$  on the appearance of viscous fingering.

In summary, the increase in  $U_{top}$  or  $R$  individually is found to suppress density fingering. However, when  $U_{top}$  and  $R$  grow to a sufficiently high level, they can jointly act as the driving force for viscous fingering.

### C. Stability analysis

Following discussions on effects of  $R$  and  $U_{top}$ , further simulations are undertaken in this section to investigate flow stability. Simulations are conducted for  $Ra = 10^9$  (case III),  $Ra = 10^8$  (case IV), and  $Ra = 10^7$  (case V), with  $U_{top} = 0-10^{-2}$  and  $R = -7-7$ , with simulation parameters being listed in Table II.

To quantitatively illustrate the fingering phenomenon, Fig. 9 demonstrates the  $l_m$  and  $t_e$  contour plots in the  $U_{top}$ - $R$  plane for cases III when fluid fronts move to  $l_f = 0.75l_y$ . Based on the values of  $l_m$ ,  $t_e$ , and fingering patterns, the parameter space is divided into five distinct

TABLE II. Parameters for cases III, IV, and V in Part C.

Tests	Rayleigh number $Ra$	Injection velocity $U_{top}$	Viscosity ratio $R$
Case III	$10^9$	$[0, 10^{-2}]$	$[-7, 7]$
Case IV	$10^8$	$[0, 10^{-2}]$	$[-7, 7]$
Case V	$10^7$	$[0, 10^{-2}]$	$[-7, 7]$

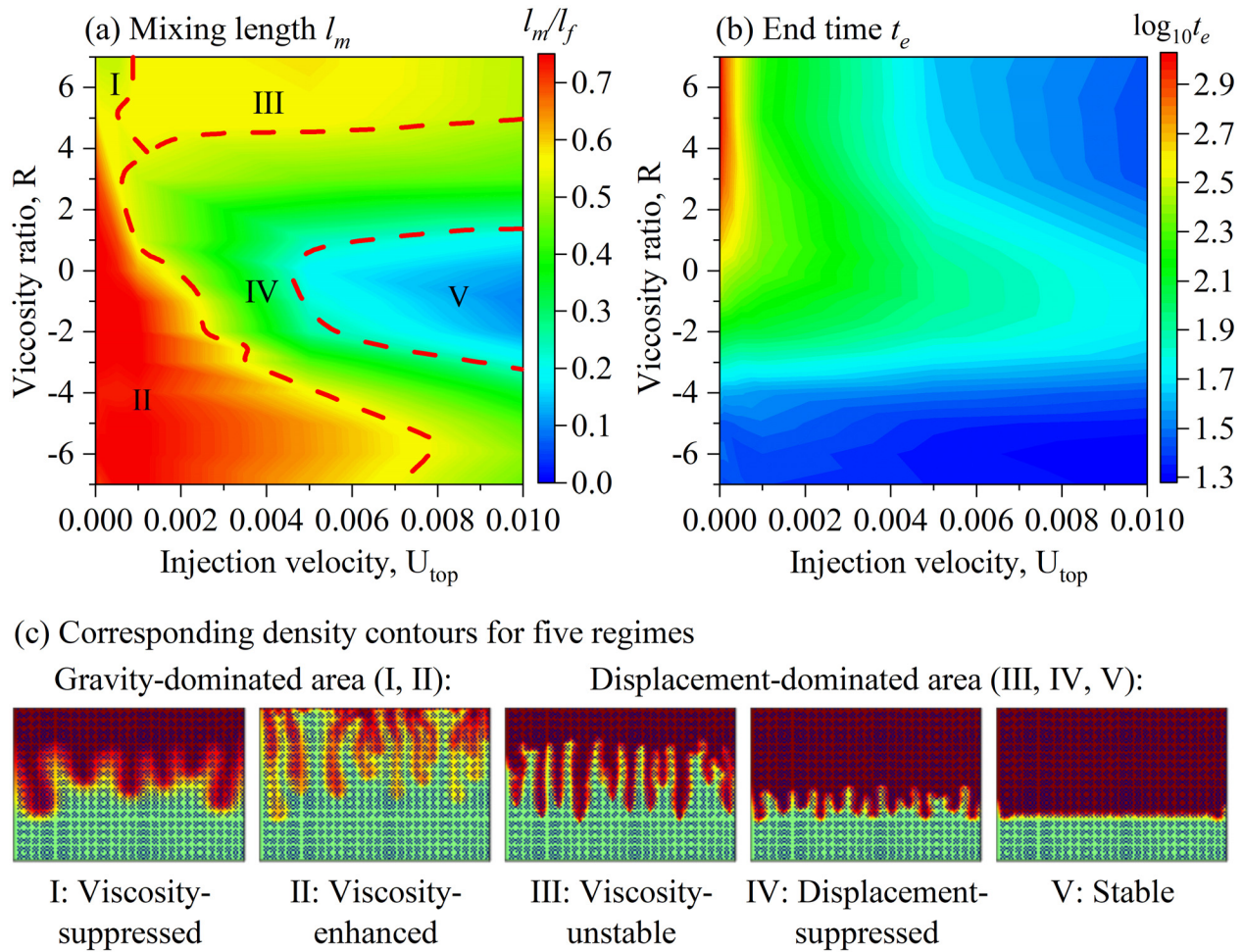


**FIG. 9.** Contours of (a) the mixing length  $l_m$  and (b) end time  $t_e$  when fluid fronts move to  $l_f = 0.75l_y$ , in the  $U_{top}$ - $R$  plane for case III with  $Ra = 10^9$ . Five distinct regimes are classified as: viscosity-suppressed (I), viscosity-enhanced (II), viscosity-unstable (III), displacement-suppressed (IV), and stable (V). (c) Corresponding density contours are presented to illustrate fingering patterns under five regimes.

regimes: viscosity-suppressed (I), viscosity-enhanced (II), viscosity-unstable (III), displacement-suppressed (IV), and stable (V). At low  $U_{top}$  values, the flow is dominated by the buoyance force  $F$ , and thus the parameter space is referred to as the gravity-dominated region. The gravity-dominated area is further divided into viscosity-suppressed (I) and viscosity-enhanced (II) regimes according to the value of  $R$ . In the viscosity-suppressed regime I, a relatively high  $R$  shortens the fingering length  $l_m$  and prolongs the duration of fingering development (i.e.,  $t_e$ ), hence suppressing fingering in area I. Conversely, in the viscosity-enhanced regime II, a small  $R$  enhances density fingering, resulting in large  $l_m$  and small  $t_e$ . As  $U_{top}$  increases, the displacement effect gradually becomes dominant in the flow, and the parameter space is defined as the displacement-dominated area. Although  $U_{top}$  suppresses density fingering to some extent, it acts as a driving force for viscous fingering. As a result, the gravity-dominated area can be divided into three regimes, namely, viscosity-unstable (III), displacement-suppressed (IV), and stable (V) regimes. In the viscosity-unstable regime III,  $U_{top}$  and  $R$  are sufficiently large to cause

viscous fingering. Consequently, the large  $l_m$  and small  $t_e$  are observed in area III. In the displacement-suppressed regime IV, density fingering is suppressed by the moderate  $U_{top}$ . In the stable regime V, the large  $U_{top}$  inhibits density fingering, while the moderate  $R$  is inadequate for inducing viscous fingering. The combination of these two factors results in a stable flow. The fingering patterns corresponding to regions I-V are depicted in Fig. 9(c).

After dividing the parameter space into five regimes according to the flow stability for cases III, similar analysis is conducted to summarize the stable and unstable regions for cases IV ( $Ra = 10^8$ ) and cases V ( $Ra = 10^7$ ). To quantitatively present the flow stability, the fingering length  $l_m/l_y$  at  $t_e$  (i.e.,  $l_f = 0.75l_y$ ) is graphed against  $R$  on the x axis,  $U_{top}$  on the y axis, and  $l_m/l_y$  on the z axis in Fig. 10. The overall flow instability increases with larger values of  $l_m/l_y$ . The aforementioned five regimes can be identified generally for other values of  $Ra$ . In addition, Fig. 10 also confirms the effects of  $U_{top}$  and  $R$  that the increasing  $U_{top}$  or  $R$  individually suppresses density fingering, while they together can gradually drive viscous fingering.

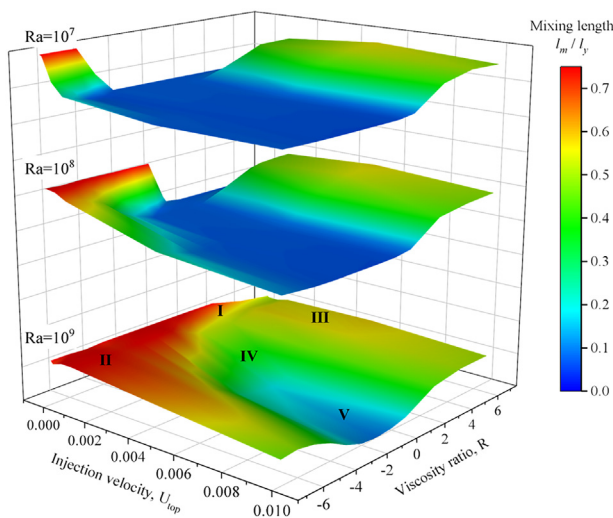


**FIG. 10.** Three-dimensional plotting of fingering length  $l_m/l_f$  in the  $U_{top}$ - $R$  plane for  $Ra = 10^7$ ,  $10^8$ , and  $10^9$  (cases V, IV, and III) with five distinct regimes labeled for  $Ra = 10^9$ .

Moreover, a close inspection of the flow regimes in cases III–V reveals the effects of  $Ra$  on the flow stability. As  $Ra$  decreases, the stable regime V expands in the parameter space, while the gravity-dominated regimes I and II contract. This is attributed to the fact that the reduced buoyance force  $F$  with the decreasing  $Ra$  degrades the density fingering intensity. Specifically, as  $Ra$  decreases from  $10^9$  to  $10^8$ , density fingering is weakened and thus part of the initially unstable regimes I and II become stabilized.

## V. CONCLUSIONS

In this work, a multiple-relaxation-time lattice Boltzmann method is utilized to study the displacements between two miscible and incompressible fluids in porous media at the pore scale. Considering the coexistence of interface instabilities (i.e., density fingering and viscous fingering), simulations are conducted for different values of Rayleigh number  $Ra$ , viscosity ratio  $R$ , and injected velocity  $U_{top}$ . Initially, the general fingering dynamics are discussed in cases without or with  $U_{top}$ . From the perspective of fingering development, the flow follows a similar route from the diffusion-dominated stage into the unstable fingering stage. For a fixed  $Ra$ , the density fingering intensity is found to be attenuated by the growing  $R$  or  $U_{top}$  due to the enhanced viscous resistance or displacement magnitude. Consequently, a large  $U_{top}$  in conjunction with a moderate  $R$  can effectively inhibit the onset of density fingering and introduce a stable flow regime. Notably, with the continuous increase in both  $U_{top}$  and  $R$ , these two parameters gradually facilitate the development of viscous fingering. In addition, the rise in  $Ra$  is shown to amplify the buoyance force and subsequently intensity of the density fingering. These fingering phenomena are investigated quantitatively by evaluating the fingering development time period  $t_e$ , density jump  $\Delta\rho$ , front position  $l_f$ , mixing length  $l_m$ , and fingering growth velocity  $U_m$ . Finally, by comparing values of  $l_m$  and  $t_e$  for each fixed  $Ra$ , five flow patterns are classified as viscosity-suppressed (I), viscosity-enhanced (II), viscosity-unstable (III), displacement-suppressed (IV), and stable (V) regimes.

This classification depends on the relative values of  $U_{top}$  and  $R$ . Moreover, a three-dimensional phase diagram spanned by  $Ra$ ,  $U_{top}$ , and  $R$  is plotted, which demonstrates the distributions and parameter ranges of the above five flow patterns.

Based on the above simulations and discussions,  $R$ ,  $U_{top}$ , and  $Ra$  are proven to have complex impacts on the interface instabilities, thereby influencing the spreading fluids. These findings have profound implications for improving the efficiency of  $CO_2$  capture and storage. Due to the limitation of the 2D system adopted, the porosity of the medium is larger than that of the realistic 3D system. To further advance this field of study, future research should be focused on the mixing process with reactions and realistic porous media in 3D.

## SUPPLEMENTARY MATERIAL

See the supplementary material for the validation of the multiple-relaxation-time lattice Boltzmann method for density instability with viscosity contrast.

## ACKNOWLEDGMENTS

Support from the UK Engineering and Physical Sciences Research Council under the project “UK Consortium on Mesoscale Engineering Sciences (UKCOMES)” (Grant No. EP/X035875/1) was gratefully acknowledged. This work made use of computational support by CoSeC, the Computational Science Centre for Research Communities, through UKCOMES.

## AUTHOR DECLARATIONS

### Conflict of Interest

The authors have no conflicts to disclose.

### Author Contributions

**Jin Chen:** conceptualization (equal); data curation (lead); formal analysis (lead); investigation (lead); methodology (lead); software (lead); validation (lead); visualization (lead); writing—original draft (lead); and writing—review and editing (equal). **Geng Wang:** investigation (supporting); methodology (supporting); software (supporting); and writing—review and editing (equal). **Junyu Yang:** methodology (supporting); software (supporting); and writing—review and editing (supporting). **Timan Lei:** conceptualization (equal); data curation (equal); formal analysis (equal); software (equal); visualization (equal); and writing—review and editing (equal). **Kai H. Luo:** methodology (equal); project administration (equal); resources (equal); software (equal); supervision (equal); and writing—review and editing (equal).

## DATA AVAILABILITY

The data that support the findings of this study are available from the corresponding authors upon reasonable request.

## APPENDIX: NUMERICAL METHOD

The evolution equations of the particle distribution function in the MRT LB model for the governing equations can be written as<sup>53–55</sup>



$$f_i(\mathbf{x} + \mathbf{e}_i \delta_t, t + \delta_t) - f_i(\mathbf{x}, t) = -(\mathbf{M}^{-1} \mathbf{S} \mathbf{M})_{ij} [f_j(\mathbf{x}, t) - f_j^{eq}(\mathbf{x}, t)] + \delta_t (\mathbf{M}^{-1} (\mathbf{I} - 0.5 \mathbf{S}) \mathbf{M})_{ij} \bar{\mathbf{F}}_j, \quad (\text{A1})$$

$$g_i(\mathbf{x} + \mathbf{e}_i \delta_t, t + \delta_t) - g_i(\mathbf{x}, t) = -(\mathbf{M}^{-1} \mathbf{S}_C \mathbf{M})_{ij} [g_j(\mathbf{x}, t) - g_j^{eq}(\mathbf{x}, t)], \quad (\text{A2})$$

for  $i, j = 0, 1, \dots, 8$  representing discrete velocity directions, where  $f_i(\mathbf{x}, t)$  and  $g_i(\mathbf{x}, t)$  are distribution functions at location  $\mathbf{x}$  and time  $t$  for the fluid density and the concentration, respectively,  $\mathbf{e}_i$  is the discrete velocity and  $\delta_t$  is the time step. The equilibrium distribution functions are defined as<sup>56</sup>

$$f_i^{eq} = w_i \left( \rho_p + \rho_0 \left( \frac{\mathbf{u} \cdot \mathbf{e}_i}{c_s^2} + \frac{(\mathbf{u} \cdot \mathbf{e}_i)^2}{2c_s^4} - \frac{\mathbf{u} \cdot \mathbf{u}}{2c_s^2} \right) \right), \quad (\text{A3})$$

$$g_i^{eq} = w_i C \left( 1 + \frac{\mathbf{u} \cdot \mathbf{e}_i}{c_s^2} + \frac{(\mathbf{u} \cdot \mathbf{e}_i)^2}{2c_s^4} - \frac{\mathbf{u} \cdot \mathbf{u}}{2c_s^2} \right), \quad (\text{A4})$$

where  $w_i$  is the weights specified to the chosen velocity set, and  $c_s$  is the lattice sound velocity.  $\rho_p$  is a variable related to the fluid pressure as  $p = c_s^2 \rho_p$ , and  $\rho_0$  is the fluid density. The distribution function for the force  $\mathbf{F}$  is defined as

$$\bar{\mathbf{F}}_i = w_i \left[ \frac{\mathbf{F} \cdot \mathbf{e}_i}{c_s^2} + \frac{(\mathbf{u} \cdot \mathbf{e}_i)(\mathbf{F} \cdot \mathbf{e}_i)}{c_s^4} - \frac{\mathbf{u} \cdot \mathbf{F}}{c_s^2} \right]. \quad (\text{A5})$$

The transformation matrix  $\mathbf{M}$  for the D2Q9 model is

$$\mathbf{M} = \begin{pmatrix} 1 & 1 & 1 & 1 & 1 & 1 & 1 & 1 & 1 \\ -4 & -1 & -1 & -1 & -1 & 2 & 2 & 2 & 2 \\ 4 & -2 & -2 & -2 & -2 & 1 & 1 & 1 & 1 \\ 0 & 1 & 0 & -1 & 0 & 1 & -1 & -1 & 1 \\ 0 & -2 & 0 & 2 & 0 & 1 & -1 & -1 & 1 \\ 0 & 0 & 1 & 0 & -1 & 1 & 1 & -1 & -1 \\ 0 & 0 & -2 & 0 & 2 & 1 & 1 & -1 & -1 \\ 0 & 1 & -1 & 1 & -1 & 0 & 0 & 0 & 0 \\ 0 & 0 & 0 & 0 & 0 & 1 & -1 & 1 & -1 \end{pmatrix}. \quad (\text{A6})$$

This matrix maps distribution functions  $\mathbf{f}$  and  $\mathbf{g}$  to the moment space  $\hat{\mathbf{f}} = \mathbf{M} \cdot \mathbf{f}$  and  $\hat{\mathbf{g}} = \mathbf{M} \cdot \mathbf{g}$ , respectively. Now, the evolution equations become

$$\hat{\mathbf{f}}(\mathbf{x} + \mathbf{e}_i \delta_t, t + \delta_t) - \hat{\mathbf{f}}(\mathbf{x}, t) = -\mathbf{S} [\hat{\mathbf{f}}(\mathbf{x}, t) - \hat{\mathbf{f}}^{eq}(\mathbf{x}, t)] + \delta_t \left( \mathbf{I} - \frac{\mathbf{S}}{2} \right) \hat{\mathbf{F}}, \quad (\text{A7})$$

$$\hat{\mathbf{g}}(\mathbf{x} + \mathbf{e}_i \delta_t, t + \delta_t) - \hat{\mathbf{g}}(\mathbf{x}, t) = -\mathbf{S}_C [\hat{\mathbf{g}}(\mathbf{x}, t) - \hat{\mathbf{g}}^{eq}(\mathbf{x}, t)], \quad (\text{A8})$$

where  $\mathbf{S}$  and  $\mathbf{S}_C$  are the diagonal relaxation factor matrices for  $\hat{\mathbf{f}}$  and  $\hat{\mathbf{g}}$ , respectively. The equilibrium distribution functions in the moment space are described as

$$\hat{\mathbf{f}}^{eq} = \left( \rho_p, -2\rho_p + 3\rho_0 u^2, \rho_p - 3\rho_0 u^2, \rho_0 u, -\rho_0 u, \rho_0 v, -\rho_0 v, \rho_0 (u^2 - v^2), \rho_0 uv \right), \quad (\text{A9})$$

$$\hat{\mathbf{g}}^{eq} = C(1, -2 + 3u^2, 1 - 3u^2, u, -u, v, -v, u^2 - v^2, uv). \quad (\text{A10})$$

The forcing moments  $\hat{\mathbf{F}}$  are described as

$$\hat{\mathbf{F}} = (0, 6\mathbf{u} \cdot \mathbf{F}, -6\mathbf{u} \cdot \mathbf{F}, F_x, -F_x, F_y, -F_y, 2(uF_x - vF_y), uF_y + vF_x). \quad (\text{A11})$$

The macroscopic fluid density, velocity, and concentration can be derived from the distribution functions as

$$\rho_p = \sum_i f_i, \quad \mathbf{u} = \left( \sum_i \mathbf{e}_i f_i + 0.5 \delta_t \mathbf{F} \right) / \rho_0, \quad C = \sum_i g_i. \quad (\text{A12})$$

Note that here in LB equations, the relaxation times  $\tau$  and  $\tau_c$  can be derived from the Chapman–Enskog analysis as<sup>57</sup>

$$\nu = c_s^2 (\tau - 0.5) \delta_t, \quad D = c_s^2 (\tau_c - 0.5) \delta_t. \quad (\text{A13})$$

As for the boundary conditions, the non-equilibrium extrapolation method is utilized for the top and bottom flows to realize the prescribed velocity and concentration<sup>56</sup>

$$f_i(\mathbf{x}, t) = f_i^{eq}(\mathbf{x}, t) + f_i(\mathbf{x}_f, t) - f_i^{eq}(\mathbf{x}_f, t), \quad (\text{A14})$$

$$g_i(\mathbf{x}, t) = g_i^{eq}(\mathbf{x}, t) + g_i(\mathbf{x}_f, t) - g_i^{eq}(\mathbf{x}_f, t), \quad (\text{A15})$$

where  $\mathbf{x}_f$  denotes the adjacent location with known distribution functions next to the boundaries. For the no-slip and no-flux boundary conditions at the solid grain surface in porous media, the halfway bounce-back method is utilized as<sup>58</sup>

$$f_i(\mathbf{x}, t + \delta_t) = f'_i(\mathbf{x}, t), \quad (\text{A16})$$

$$g'_i(\mathbf{x}, t + \delta_t) = g'_i(\mathbf{x}, t), \quad (\text{A17})$$

where  $e'_i = -e_i$ , with  $e_i$  pointing to the solid grains, and  $f'_i(\mathbf{x}, t)$  and  $g'_i(\mathbf{x}, t)$  representing the post-collision distribution functions.

## REFERENCES

- <sup>1</sup>N. Oreskes, “The scientific consensus on climate change,” *Science* **306**(5702), 1686 (2004).
- <sup>2</sup>J. Rogelj *et al.*, “Paris agreement climate proposals need a boost to keep warming well below 2 °C,” *Nature* **534**(7609), 631–639 (2016).
- <sup>3</sup>S. Pye *et al.*, “Achieving net-zero emissions through the reframing of UK national targets in the post-Paris agreement era,” *Nat. Energy* **2**(3), 17024 (2017).
- <sup>4</sup>M. A. Celia, “Geological storage of captured carbon dioxide as a large-scale carbon mitigation option,” *Water Resour. Res.* **53**(5), 3527–3533, <https://doi.org/10.1002/2017WR020841> (2017).
- <sup>5</sup>J. Ennis-King and L. Paterson, “Role of convective mixing in the long-term storage of carbon dioxide in deep saline formations,” *SPE J.* **10**, 349–356 (2005).
- <sup>6</sup>H. E. Huppert and J. A. Neufeld, “The fluid mechanics of carbon dioxide sequestration,” *Annu. Rev. Fluid Mech.* **46**(1), 255–272 (2014).
- <sup>7</sup>S. M. Benson and F. M. Orr, “Carbon dioxide capture and storage,” *MRS Bull.* **33**(4), 303–305 (2008).
- <sup>8</sup>T. J. Kneafsey and K. Pruess, “Laboratory flow experiments for visualizing carbon dioxide-induced, density-driven brine convection,” *Transp. Porous Media* **82**(1), 123–139 (2010).
- <sup>9</sup>T. J. Kneafsey and K. Pruess, “Laboratory experiments and numerical simulation studies of convectively enhanced carbon dioxide dissolution,” *Energy Procedia* **4**, 5114–5121 (2011).
- <sup>10</sup>Y. Chen *et al.*, “Inertial effects during the process of supercritical CO2 displacing brine in a sandstone: Lattice Boltzmann simulations based on the continuum-surface-force and geometrical wetting models,” *Water Resour. Res.* **55**(12), 11144, <https://doi.org/10.1029/2019WR025746> (2019).
- <sup>11</sup>Y. Teng *et al.*, “An experimental study of density-driven convection of fluid pairs with viscosity contrast in porous media,” *Int. J. Heat Mass Transfer* **152**, 119514 (2020).

- <sup>12</sup>H. Emami-Meybodi, "Stability analysis of dissolution-driven convection in porous media," *Phys. Fluids* **29**(1), 014102 (2017).
- <sup>13</sup>H. Emami-Meybodi *et al.*, "Convective dissolution of CO<sub>2</sub> in saline aquifers: Progress in modeling and experiments," *Int. J. Greenhouse Gas Control* **40**, 238–266 (2015).
- <sup>14</sup>H. Erfani, M. Babaei, and V. Niasar, "Signature of geochemistry on density-driven CO mixing in sandstone aquifers," *Water Resour. Res.* **56**(3), e2019WR026060, <https://doi.org/10.1029/2019WR026060> (2020).
- <sup>15</sup>H. Erfani, M. Babaei, and V. Niasar, "Dynamics of CO<sub>2</sub> density-driven flow in carbonate aquifers: Effects of dispersion and geochemistry," *Water Resour. Res.* **57**(4), e2020WR027829, <https://doi.org/10.1029/2020WR027829> (2021).
- <sup>16</sup>D. A. Bratsun, A. I. Mizev, and E. A. Mosheva, "Extended classification of the buoyancy-driven flows induced by a neutralization reaction in miscible fluids. Part 2. Theoretical study," *J. Fluid Mech.* **916**, A23 (2021).
- <sup>17</sup>A. I. Mizev, E. A. Mosheva, and D. A. Bratsun, "Extended classification of the buoyancy-driven flows induced by a neutralization reaction in miscible fluids. Part 1. Experimental study," *J. Fluid Mech.* **916**, A22 (2021).
- <sup>18</sup>A. Riaz *et al.*, "Onset of convection in a gravitationally unstable diffusive boundary layer in porous media," *J. Fluid Mech.* **548**(1), 87 (2006).
- <sup>19</sup>S. M. Raad and H. Hassanzadeh, "Onset of dissolution-driven instabilities in fluids with nonmonotonic density profile," *Phys. Rev. E* **92**(5), 053023 (2015).
- <sup>20</sup>T. Lei and K. H. Luo, "Pore-scale simulation of miscible viscous fingering with dissolution reaction in porous media," *Phys. Fluids* **33**(3), 034134 (2021).
- <sup>21</sup>L. Ju *et al.*, "Pore-scale study of miscible density-driven mixing flow in porous media," *Phys. Fluids* **33**(3), 034113 (2021).
- <sup>22</sup>M. A. Nomeli and A. Riaz, "A data driven model for the impact of IFT and density variations on CO<sub>2</sub> storage capacity in geologic formations," *Adv. Water Resour.* **107**, 83–92 (2017).
- <sup>23</sup>D. Daniel, A. Riaz, and H. A. Tchelepi, "Onset of natural convection in layered aquifers," *J. Fluid Mech.* **767**, 763–781 (2015).
- <sup>24</sup>D. Daniel, N. Tilton, and A. Riaz, "Optimal perturbations of gravitationally unstable, transient boundary layers in porous media," *J. Fluid Mech.* **727**, 456–487 (2013).
- <sup>25</sup>S. S. Gopalakrishnan, B. Knaepen, and A. De Wit, "Scalings of the mixing velocity for buoyancy-driven instabilities in porous media," *J. Fluid Mech.* **914**, A27 (2021).
- <sup>26</sup>O. Manickam and G. M. Homsy, "Stability of miscible displacements in porous media with nonmonotonic viscosity profiles," *Phys. Fluids A* **5**(6), 1356–1367 (1993).
- <sup>27</sup>O. Manickam and G. M. Homsy, "Fingering instabilities in vertical miscible displacement flows in porous media," *J. Fluid Mech.* **288**(1), 75–102 (1995).
- <sup>28</sup>G. K. Koskuner and R. G. Bentsen, "An extended theory to predict the onset of viscous instabilities for miscible displacements in porous media," *Transp. Porous Media* **5**(5), 473–490 (1990).
- <sup>29</sup>J. M. Dumore, "Stability considerations in downward miscible displacements," *Soc. Pet. Eng. J.* **4**, 356–362 (1964).
- <sup>30</sup>S. Hill and F. I. P. F.S.S., "Channeling in packed columns," *Chem. Eng. Sci.* **1**(6), 247–253 (1952).
- <sup>31</sup>M. A. Mahardika *et al.*, "Competition of gravity and viscous forces in miscible vertical displacement in a three-dimensional porous medium," *Phys. Fluids* **34**(7), 073102 (2022).
- <sup>32</sup>M. A. Amooie, M. R. Soltanian, and J. Moortgat, "Solutal convection in porous media: Comparison between boundary conditions of constant concentration and constant flux," *Phys. Rev. E* **98**(3), 033118 (2018).
- <sup>33</sup>A. De Wit, "Miscible density fingering of chemical fronts in porous media: Nonlinear simulations," *Phys. Fluids* **16**(1), 163–175 (2004).
- <sup>34</sup>R. Khosrokhavar, *Effect of Salinity and Pressure on the Rate of Mass Transfer in Aquifer Storage of Carbon Dioxide* (Springer International Publishing, 2016), pp. 33–47.
- <sup>35</sup>G. M. Homsy, "Viscous fingering in porous media," *Annu. Rev. Fluid Mech.* **19**(1), 271–311 (1987).
- <sup>36</sup>C. T. Tan and G. M. Homsy, "Simulation of nonlinear viscous fingering in miscible displacement," *Phys. Fluids* **31**(6), 1330–1338 (1988).
- <sup>37</sup>O. Manickam and G. M. Homsy, "Simulation of viscous fingering in miscible displacements with nonmonotonic viscosity profiles," *Phys. Fluids* **6**(1), 95–107 (1994).
- <sup>38</sup>T. Lei, X. Meng, and Z. Guo, "Pore-scale study on reactive mixing of miscible solutions with viscous fingering in porous media," *Comput. Fluids* **155**, 146–160 (2017).
- <sup>39</sup>B. Dastvareh and J. Azaiez, "Instabilities of nanofluid flow displacements in porous media," *Phys. Fluids* **29**(4), 044101 (2017).
- <sup>40</sup>S. Sarkar, S. Ganguly, and M. Mishra, "Single diffusive magnetohydrodynamic pressure driven miscible displacement flows in a channel," *Phys. Fluids* **31**(8), 082102 (2019).
- <sup>41</sup>A. De Wit and G. M. Homsy, "Viscous fingering in periodically heterogeneous porous media. II. Numerical simulations," *J. Chem. Phys.* **107**(22), 9619–9628 (1997).
- <sup>42</sup>S. A. Abdul Hamid and A. H. Muggeridge, "Fingering regimes in unstable miscible displacements," *Phys. Fluids* **32**(1), 016601 (2020).
- <sup>43</sup>D. Keable *et al.*, "The effect of viscosity ratio and Peclet number on miscible viscous fingering in a Hele-Shaw cell: A combined numerical and experimental study," *Transp. Porous Media* **143**(1), 23–45 (2022).
- <sup>44</sup>T. Lei and K. H. Luo, "Pore-scale study of coke formation and combustion in porous media using lattice Boltzmann method," *Proc. Combust. Inst.* **39**(4), 5591–5599 (2023).
- <sup>45</sup>T. Lei *et al.*, "Study of CO<sub>2</sub> desublimation during cryogenic carbon capture using the lattice Boltzmann method," *J. Fluid Mech.* **964**, A1 (2023).
- <sup>46</sup>R. Liyanage *et al.*, "Direct experimental observations of the impact of viscosity contrast on convective mixing in a three-dimensional porous medium," *Phys. Fluids* **32**(5), 056604 (2020).
- <sup>47</sup>Q. Xu *et al.*, "Pore-scale modelling of the coupled thermal and reactive flow at the combustion front during crude oil in-situ combustion," *Chem. Eng. J.* **350**, 776–790 (2018).
- <sup>48</sup>Q. Li *et al.*, "Lattice Boltzmann methods for multiphase flow and phase-change heat transfer," *Prog. Energy Combust. Sci.* **52**, 62–105 (2016).
- <sup>49</sup>E. A. Spiegel and G. Veronis, "On the Boussinesq approximation for a compressible fluid," *Astrophys. J.* **131**, 442 (1960).
- <sup>50</sup>N. Rakotomalala, D. Salin, and P. Watzky, "Miscible displacement between two parallel plates: BGK lattice gas simulations," *J. Fluid Mech.* **338**, 277–297 (1997).
- <sup>51</sup>R. Du, B. Shi, and X. Chen, "Multi-relaxation-time lattice Boltzmann model for incompressible flow," *Phys. Lett. A* **359**(6), 564–572 (2006).
- <sup>52</sup>J. S. Nijjer, D. R. Hewitt, and J. A. Neufeld, "Stable and unstable miscible displacements in layered porous media," *J. Fluid Mech.* **869**, 468–499 (2019).
- <sup>53</sup>T. Lei, Z. Wang, and K. H. Luo, "Study of pore-scale coke combustion in porous media using lattice Boltzmann method," *Combust. Flame* **225**, 104–119 (2021).
- <sup>54</sup>P. Lallemand and L.-S. Luo, "Theory of the lattice Boltzmann method: Dispersion, dissipation, isotropy, Galilean invariance, and stability," *Phys. Rev. E* **61**(6), 6546 (2000).
- <sup>55</sup>T. Lei and K. H. Luo, "Pore-scale study of dissolution-driven density instability with reaction A+B→C in porous media," *Phys. Rev. Fluids* **4**(6), 063907 (2019).
- <sup>56</sup>H. K. T. Krüger, A. Kuzmin, O. Shardt, G. Silva, and E. M. Viggien, *The Lattice Boltzmann Method: Principles and Practice* (Springer, 2017).
- <sup>57</sup>Z. Guo and C. Zheng, *Theory and Applications of Lattice Boltzmann Method* (Science Press, 2008).
- <sup>58</sup>T. Zhang *et al.*, "General bounce-back scheme for concentration boundary condition in the lattice-Boltzmann method," *Phys. Rev. E* **85**(1), 016701 (2012).